NUMERICAL AND EXPERIMENTAL INVESTIGATION OF A COOLING CONCEPT FOR AN ELECTRIC PROPULSION SYSTEM FOR AEROBATIC AIRCRAFTS

Xinying Liu*, Flavio Ferrari*, Leonardo Manfriani*
*** Centre for Aviation, School of Engineering, Zurich University of Applied Sciences**

Keywords: *electric propulsion, aerobatic aircraft, conjugate heat transfer analysis full scale wind tunnel test*

Abstract

This paper presents the development of a cooling concept for an electric propulsion system of an aerobatic aircraft. The numerical part of this paper focuses on the battery cooling performance requirements, the internal design of the cooling duct and their influence on heat transfer efficiency, using conjugate heat transfer (CHT) simulation. The analysis was performed with the computational fluid dynamics (CFD) code Ansys CFX, using a Shear Stress Transport (SST) model. It is planned to prove the cooling concept in a full scale wind tunnel test. The test preparation is also described in this paper.

1 Introduction

Some new designs for electrically powered aerobatic aircraft have recently been presented. Owing to the high noise loading of conventionally driven aerobatic aircraft, a significant sales potential is expected for aircraft equipped with high-powered electric drives. On the basis of the current aerobatic aircraft design Votec 221 (see Fig. 1) by MSW Aviation, a high performance electrically powered version for the aerobatic model is being developed. The research presented in this paper aims to explore new and efficient possibilities for powertrain cooling. The project is supported by the Swiss Federal Innovation Agency (Innosuisse).

The CAD model of the aircraft is presented in Fig. 2 and 3. The electric motor, the two inverters and the battery pack must be optimally cooled with air. This electric drive has a total efficiency of 70%, which results in a power dissipation of 70 kW at the full engine power output of 230 kW. Further, the effect of the propeller in the various flight attitudes, in combination with an electric motor is not known today. The investigation of the optimum operating point of the propeller, as well as its aerodynamic impact on the aircraft in the different attitudes, is also part of this research project.

Fig. 1. Evolaris Votec 221.

In the first phase of the project, two configurations of cooling ducts, including inlet and outlet, was defined by the Centre for Aviation of the ZHAW - Zurich University of Applied Sciences. This paper discusses the parallel cooling concept, where the cooling ducts for motor (blue) and batteries (brown) are constructed separately (see Fig. 2). Due to the high physical complexity of the whole model, in the preliminary design phase the model shown in Fig. 1 has been divided into three parts: propeller, motor cooling and battery cooling. In a previous paper [1] an unsteady Reynolds-averaged Navier-Stokes simulation (URANS) for the propeller was carried out in order to determine the optimal positions for the cooling

duct inlets. This paper focuses on battery cooling.

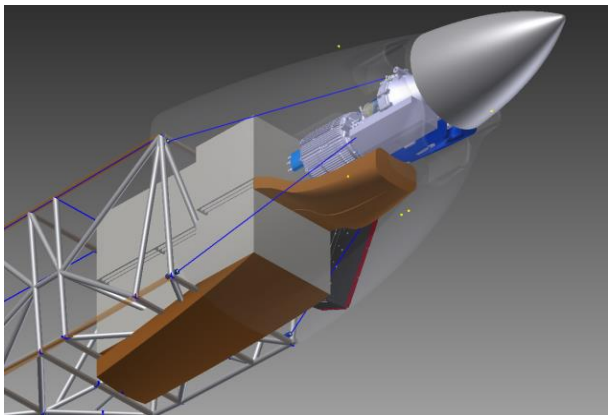

Fig. 2. CAD model of the battery, motor and gearbox.

As is well-known, compared to laminar flow, turbulent flow has an additional mechanism of heat transfer in the radial and azimuthal directions. This is commonly termed "eddy transport", which provides much better heat transfer of energy across the flow in longitudinal direction than in laminar flow. In the previously mentioned paper, many geometry variations were performed for the internal cooling passages of the fluid channel, similarly to the film cooling for gas turbine blades. Several types of geometries to increase turbulence (turbulators), e.g. pin fins [8], flow channelling, dimples and different types of ripped fluid channel [2] were investigated in experiments and numerical calculations. However, turbulators have the effect of increasing flow resistance in the fluid channel. Because of the thin internal fluid channel (3 mm) and of the high aspect ratio (85) of the cooling channel cross section for the batteries, the increase in flow resistance caused by a ripped fluid channel could overwhelm the gain in the heat transfer efficiency. Because of the geometries of the cooling channel, the heat transfer performance of a pin fin matrix is deemed to be more adequate and is presented in this paper.

Full scale wind tunnel tests of the propulsion unit installed on the aircraft are planned for February 2019. The measured results will be compared with the numerically calculated values. Wind tunnel tests aim to obtain an overall optimum solution and adjustment of the existing propeller and cooling duct as well as a statement about the potential of the simulation model.

2 Numerical procedure

2.1 Quantities of convection heat transfer

A key problem of convection heat transfer is the determination of the heat flux $\dot{q}$ at a surface exposed to a flow. The heat transfer coefficient (HTC) α can be quantified by wall temperature T_w and by the bulk temperature T_B, which is used in internal forced convection situations, and is defined as:

$$\alpha = \frac{\dot{q}}{T_w - T_B} \tag{1}$$

In general, the bulk temperature is the rate of fluid enthalpy through a cross section in a channel, divided by the rate of heat capacity through the cross section. Therefore, bulk temperature can be expressed as:

$$T_B = \frac{\int \rho u c_p T \, dA}{\int \rho u \, dA} \tag{2}$$

where ρ: fluid density, c_p: heat capacity, u: local velocity through the considered cross section A.

The three variables are spatially dependent. In the post processing part of this paper, bulk temperature will be computed as a mass flow averaged temperature at different cross sections in a single fluid channel. Another key dimensionless parameter which characterises convective heat transfer is the Nusselt number Nu, defined as the ratio of convective to conductive heat transfer across the boundary . It is defined as:

$$Nu = \frac{\alpha L}{\lambda} \tag{3}$$

where L is characteristic length (e.g. diameter for pipes and hydraulic diameter for non-circular channels), and λ is the thermal conductivity of the fluid.

2.2 Numerical methods

Conjugate heat transfer (CHT) simulations using the solver ANSYS CFX, release 18.0, were performed in this study. CHT simulations are fundamental in considering the mutual effect between coolant circuit and solid regions. The heat fluxes are then applied as thermal boundary conditions in the CHT model, where the solid component (battery cells) are simulated together with the cooling air, in order to properly evaluate both the battery cell temperature field and the heat removed by the coolant. The solid and fluid domains are connected by a thin interface. Its mass and momentum have been set to *conservative interface flux* [11], so that physics of different domain types can be defined across the interface. The data exchange between the different domains must be performed at least twice in order to meet the convergence in terms of temperatures calculated by the CHT model [12]. Due to the complexity of the physics at the boundaries, the boundary layer mesh from the fluid side should be fine enough to capture the heat transfer effect. This will be discussed in the next section.

For the fluid domain, one of the most effective turbulence models, SST [4], has been used. It is based on the solution of a turbulence / frequency based model k-ω at the wall and k-ε in the bulk flow [5]. SST has been studied in many CHT simulations, e.g. [3], [8] and [9]. It gives the most accurate heat transfer prediction for industry applications. Another important topic in turbulence modelling is the numerical treatment of the near wall region. For SST in ANSYS CFX, the wall boundary treatment exploits the simple and robust near-wall formulation of the k-ω model and switches automatically from a low-Reynolds number formulation to a wall function treatment based on grid density [11].

2.3 Preprocessing

This paper aims to discuss heat transfer performance in the narrow fluid channels, to reduce the calculation effort and to focus on this key part of battery's heat transfer performance. The simulation model, which is presented in Fig. 3, is abstracted from the whole model. It includes six battery cells, one inlet cooling duct and two outlet cooling ducts (transparent) on the top and bottom sides. Each battery cell consists of two battery plates (yellow) and three cooling air channels. All fluid channels are interconnected (grey), the so called main fluid domain is described in the following paragraphs.

A hexahedron / tetrahedron hybrid mesh was created for the CHT simulation. Because of the simple and "sweepable" geometries, domains 1, 2, 4 und 5 as well have been meshed with hexahedron structured elements. In the main fluid domain finer tetrahedron unstructured elements were used (see Tab. 1).

domain	property	mesh type	prism layer
1	fluid	hexahedron	no
2	fluid	hexahedron	no
3	fluid	tetrahedron	yes
4	fluid	hexahedron	no
5	solid	hexahedron	no

Tab. 1. Mesh domains

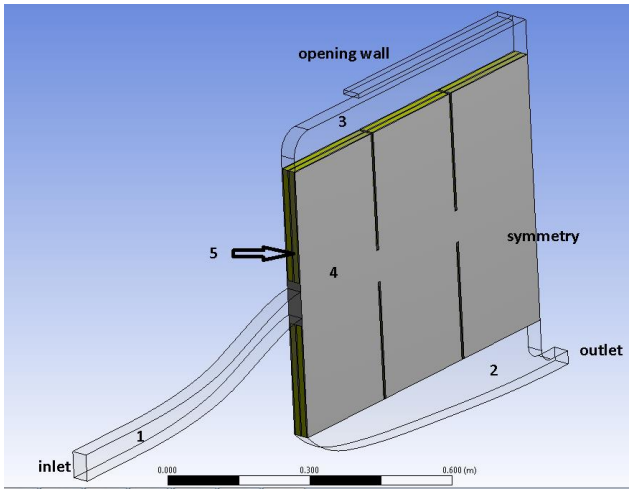

Fig. 3. Simulation model.

The mesh refinement engine *curvature and proximity* [6] has been applied to the main fluid domain, so that the details at local regions of the narrow fluid channels, which have an aspect ratio of 85, can be properly captured. With this mesh method the simple geometry area in the middle of the main fluid domain has been kept coarser in an effort to reduce computation time. As mentioned before, the near-wall regions should have a fine mesh. Prism layers have been created on the solid-fluid interface from the

main fluid side. In order to reduce the total number of elements numbers of the simulation model, the mesh of the solid domain is coarser than that of the main fluid domain, because the physics of a solid domain is simpler and must just deliver the correct temperature gradient to the interface. The general grid interface (GGI) [6] approach is used to no-match interfaces. A sectional view of the mesh is shown in Fig. 4.

In the simulations of this paper the boundary conditions are taken from the previous papers [2] and [12]. In [2] the performance of the propeller was investigated. The "worst case" with a 40 m/s cooling airspeed at the inlet is considered. In [12] the properties of the lithium-ion battery cells (a time history of battery temperature during a 20 minute aerobatic program) have been measured by an experiment. The peak battery plates temperature of 70°C was chosen as an initial value for the steady simulations. The values of thermal conductivity ($30.4\ \mathrm{W/m \cdot K}$) and of the dissipated power density ($10^5\ \mathrm{W}/m^3$) have also been derived from the previous study.

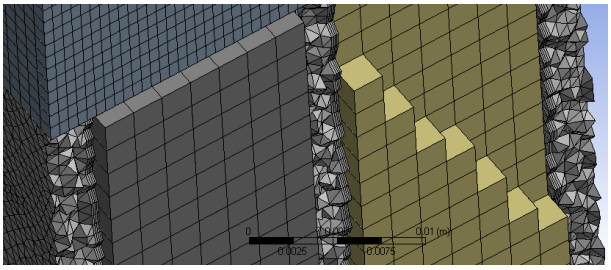

Fig. 4. Sectional view of the mesh.

2.4 Mesh study

In this section a mesh independent study is performed. The element size of the solid-fluid domain and the thickness of the first prism layer were set as input parameters. Three different mesh sizes have been tested in this study, they are listed in Tab. 2.

In Fig. 5-7 the temperature distributions on the middle section of the model are shown. In general, the three distributions look similar. It can be seen that the peak value is well below the desired upper limit of 65°C, even though the heat transfer is not optimal in the second row of the battery cells, particularly in the first two columns. This is explained by the higher flow resistance in this region. The flow there is strongly deflected and forced towards the outlet. The optimization of the outlet shape is however not the topic in this paper. The internal turbulators will be created only on the last cell of the first row (called target cell in the following sections), where the cooling air has a lower resistance compared to the current outlet shape design.

	mesh 1	mesh 2	mesh 3
element size $[m]$	$2e^{-3}$	$1e^{-3}$	$1e^{-3}$
first layer thickness $[m]$	$1e^{-4}$	$1e^{-4}$	$5e^{-5}$
Averaged y^+	8	4.2	2.1
total elements number	23 M	82 M	115 M

Tab. 2. Mesh parameters.

The velocity distribution along the black line (see Fig. 8), the bulk temperature distribution along the middle channel of target cell and heat transfer coefficient along the green lines on the surface of this channel (see Fig. 9) are chosen as criterion in the mesh study. The bulk temperatures at 10 cross sections (orange) in the observed channel are calculated and plotted against the y position. The discrete bulk values of local bulk temperature are approximated by spline. In Fig. 8 and Fig. 10 the results show only slight small differences between the 3 different mesh configurations. It can be concluded that the element size of mesh 1 is sufficient for predicting basic quantities. However, the first layer thickness is not low enough.

It can be seen in Fig. 10 and Fig. 11 that there is no significant difference between mesh 2 and 3. Further, the left side of the observed fluid channel has a higher averaged HTC than the right side.

Based on these considerations, mesh 2 was selected for further simulations.

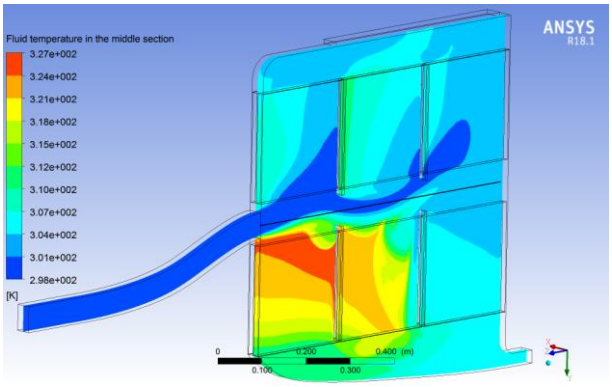

Fig. 5. Temperature distribution of mesh 1

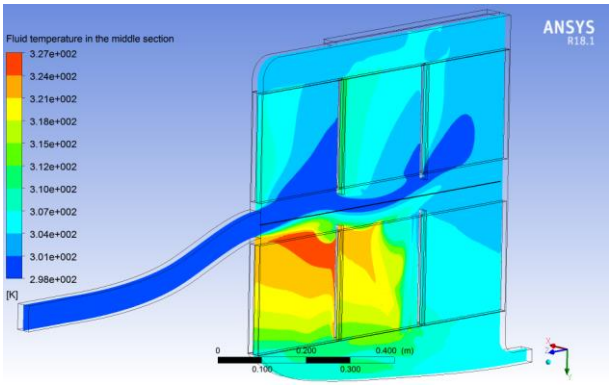

Fig. 6. Temperature distribution of mesh 2.

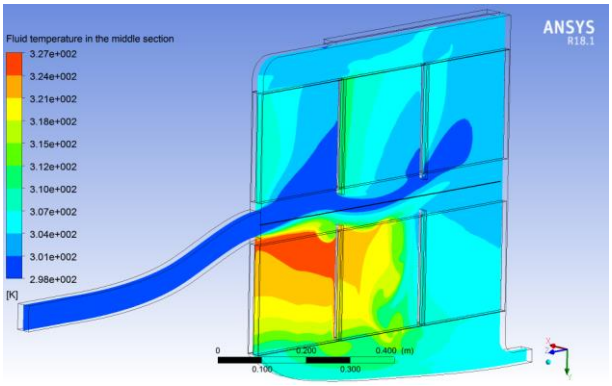

Fig. 7. Temperature distribution of mesh 3.

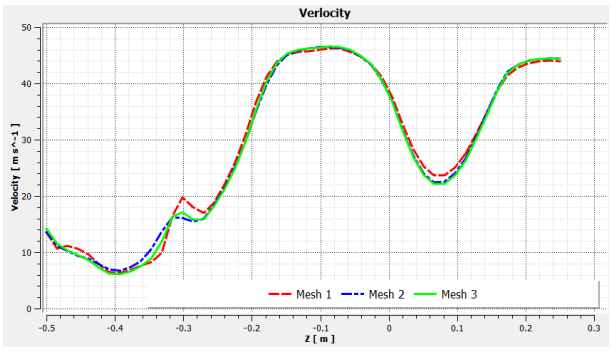

Fig. 8. Velocity distribution.

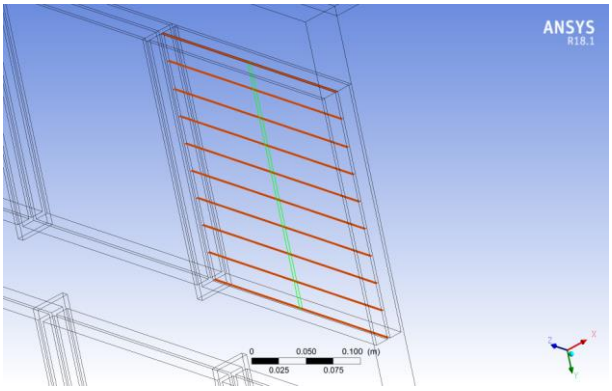

Fig. 9. Cross sections along middle fluid channel.

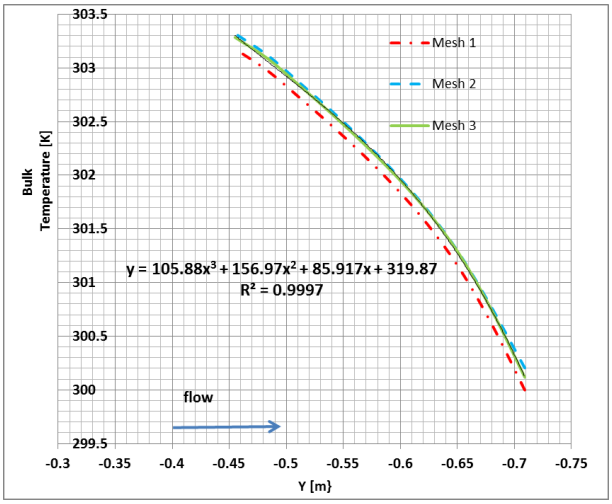

Fig. 10. Bulk temperature distribution.

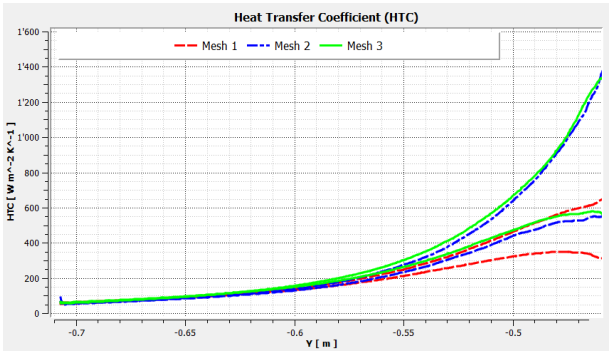

Fig. 11. Heat transfer coefficient on solid fluid interface.

2.5 New design of the cooling channel

For the new design a pin fins matrix has been placed in the fluid channel. Normally, the pin fins are arranged as showed in Fig. 12. According to past research of different geometries, the diameter *D* of the pins, the distances across *S* and in the flow direction *X* have a significant influence on the efficiency of convective heat transfer. In [3], [13] and [14]

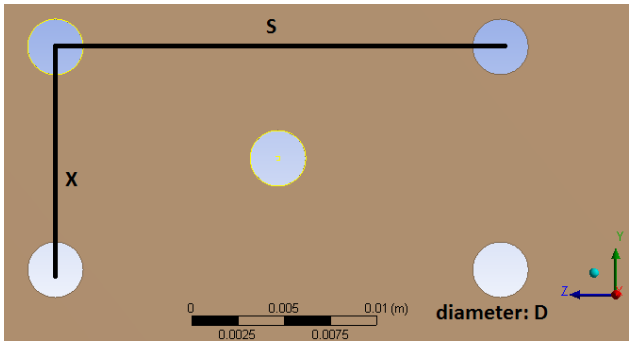

Fig. 12. Pin fins matrix

the ratio between channel height H and pin diameter D is around 1. This value was also chosen in this work as it was shown to be sufficiently effective. In [13] it was found that $S/D = 3.125$ and $X/D = 2.5$ are more suitable than other values of the distances. However, this work deals with a much higher aspect ratio of the cooling channel. $S/D = 8$ and $X/D = 4$ have been used for the basis configuration of the new design. It was determined in [1] that up to the 4^{th} and 5^{th} rows in flow direction the heat transfer apparently benefited from the vortex system around the pins and that the averaged heat transfer coefficient from 10^{th} row remains constant. Nonetheless, more rows of pin fins may increase resistance in the channel. In this work a 7x8 matrix has been chosen for the new design.

The Nusselt number distributions on the interface of middle fluid channel are presented in Fig. 13. The region with relatively high Nusselt number (red zone) of the new design is clearly larger than the original design and extended towards the pin fin matrix. Further, streamwise above the fins matrix the convective heat transfer performance was also improved. The vortex system structure around the pin is shown in Fig. 14 and Fig. 15. The flow stagnates in front of the pins. Surrounding the pins, a u-shaped lateral vortex, so called "horseshoe vortex" [7] is formed. Behind the pins two counter-rotating vortices are present. In longitudinal direction, the well-known Kármán vortex street can be predicted. Further, the pin fin matrix works as a series of subcritical convergent-divergent nozzles because of the local streamwise cross section contraction and expansion. The cooling air accelerates and decelerates frequently in the pin fin matrix. In Fig. 16 the benefit of the vortex system and flow field can been confirmed by the HTC distribution peaks along the black line (see Fig. 13). A local maximal HTC increase by 30 % can be observed, while a 50 % increase in local wall shear is predicted by the simulation. The streamwise vortices behind the matrix align again with the laminar flow, so that the HTC lines match at the end of fluid channel.

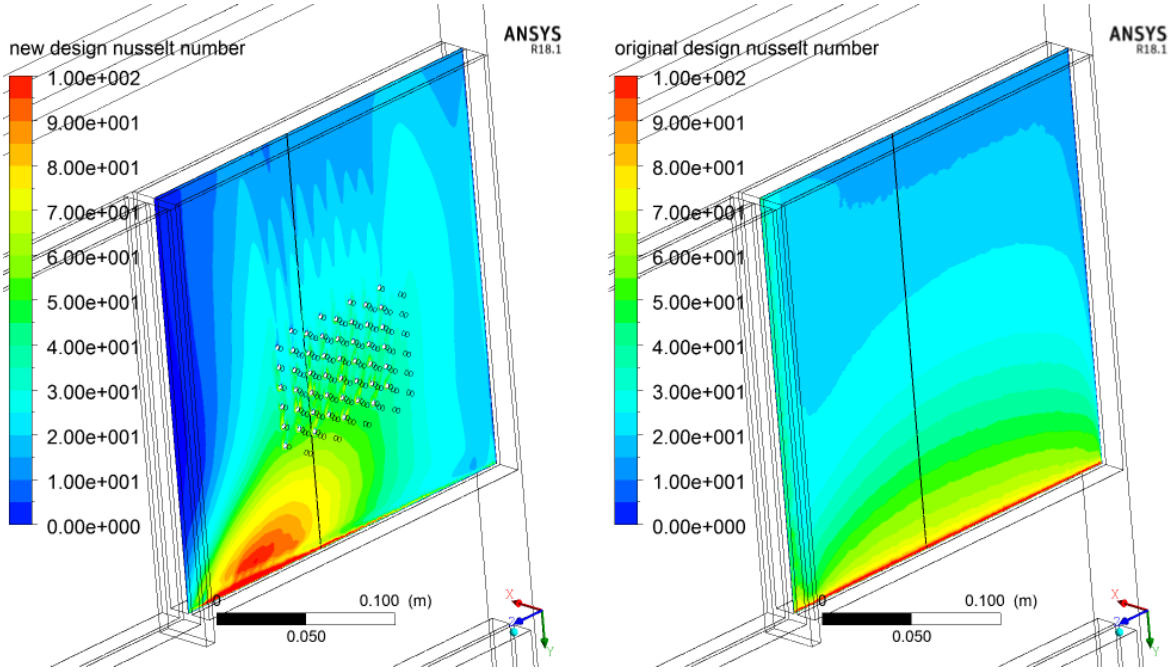

Fig. 13. Nusselt number distribution solid fluid interface.

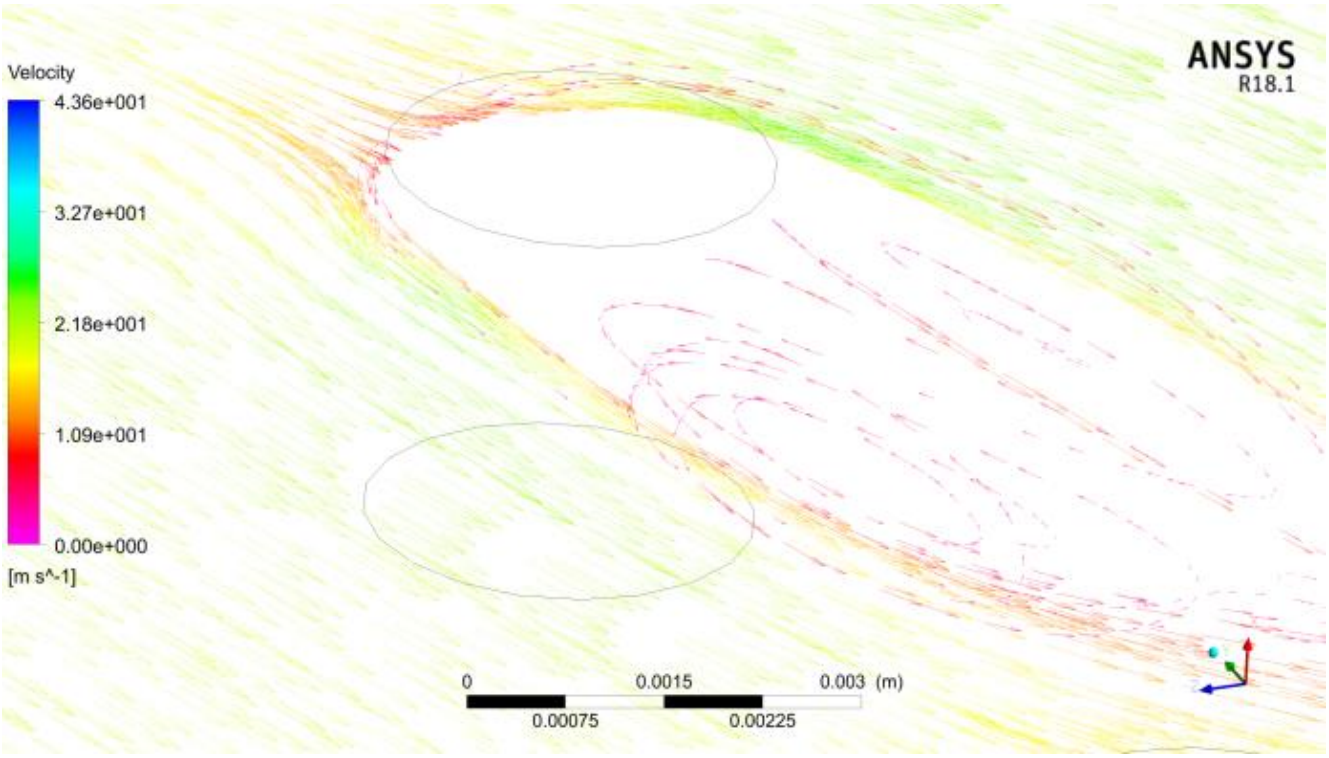

Fig. 14. Velocity vector surrounding pin fin.

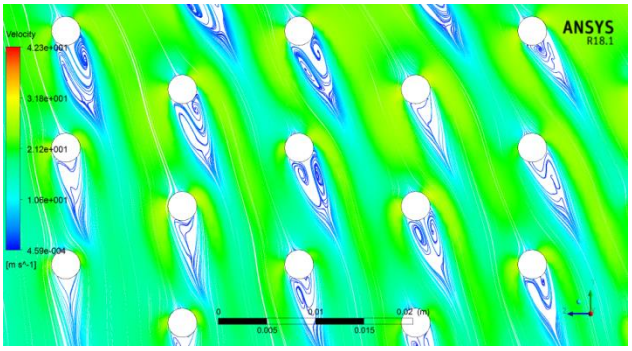

Fig. 15. Vortices around pin fins.

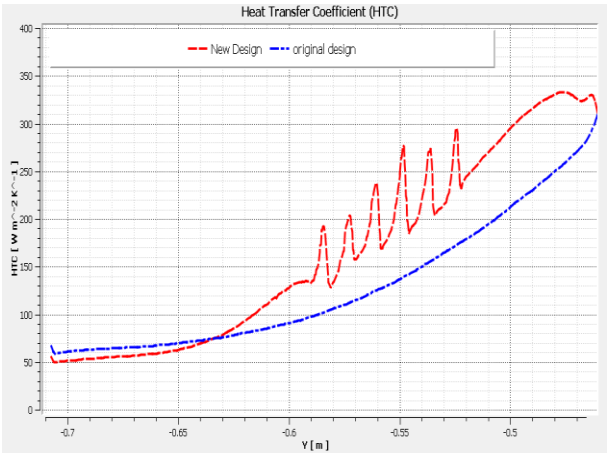

Fig. 16. Comparison of heat transfer coefficient on solid-fluid interface.

3 Wind Tunnel Testing

The CFD simulation of the whole model will be validated with wind tunnel measurements.

3.1 Model

To achieve the best result, a one to one, 6.3 m span model will be equipped with all necessary sensors and placed in the Large Wind Tunnel Emmen (LWTE) as shown in Fig. 17.

With its test section dimension of 7 m x 5 m and maximum velocity of 68 m/s, this facility fits the requirements. Since the measurement concerns only the area of the propeller and the motor housing and not the whole aircraft, blockage effects can be neglected.

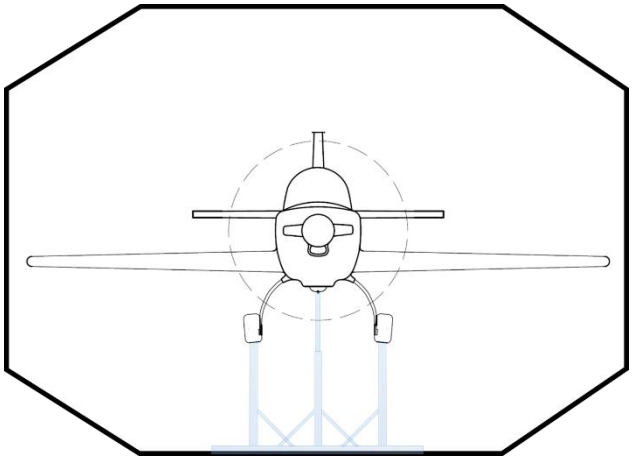

Fig. 17. Placement of aircraft in the LWTE, front view.

3.3 Parameters and Measurement Equipment

To allow a comparison with the numerical simulations of the whole model, two different parameters shall be measured: the temperature distribution on the motor, gearbox and the battery pack and the volume flow on all three inlets and all three outlets.

To measure the temperature in the battery pack, the temperature sensors of each battery cell are used. Considering 50 cells, the temperature distribution in the whole pack can be measured accurately enough.

The temperature distribution of the motor and gearbox will be measured with platinum measuring resistors placed on the surface as shown in Fig. 18. These sensors have a measurement range of -200 °C to 850 °C and an accuracy of around ± 0.5 °C at 0 °C [15].

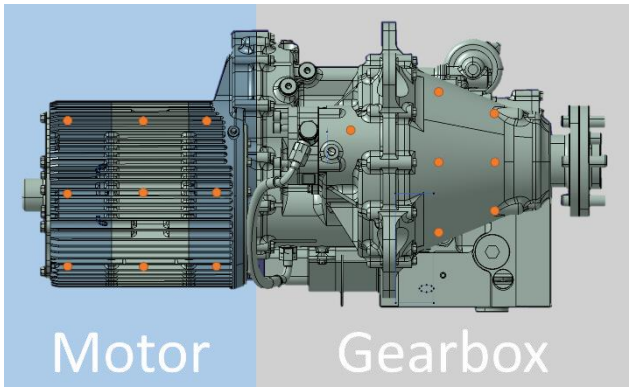

Fig. 18. Temperature sensor (orange dots) distribution on motor and gearbox.

15 sensors will be placed in rows of three evenly over the case of the motor. Twelve are placed in rows of two evenly over the front part of the gearbox and two more on its rear part, opposite to each other.

To measure static and total pressure, and therefore calculate the air flow velocity, a unit of three total-pressure tubes and six static pressure ports will be placed at every inlet and outlet. Representative for every unit, a schematic example of an inlet is shown in Fig. 19.

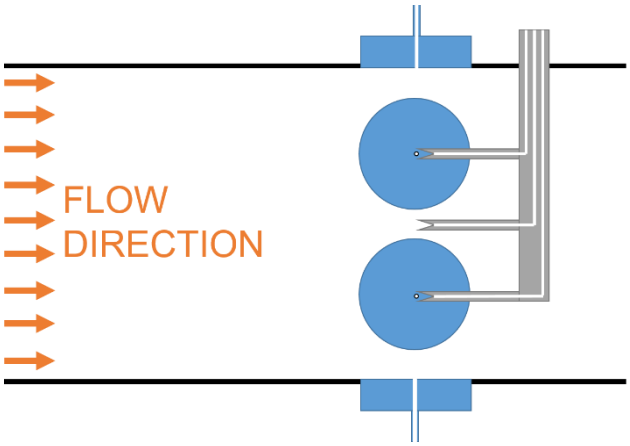

Fig. 19. Schematic top view of one measurement unit, consisting of three total-pressure tubes (blue) and three static pressure ports (grey)

All static pressure ports of one unit are physically connected to one sensor port. Hence, the average static pressure will be measured.

As Rayle [16] states, the measurement error increases with the hole diameter of a static pressure port. However, the smaller the holes, the easier they get blocked by dust and a diameter below 0.5 mm can cause severe pressure lag [3]. Therefore, a hole diameter of 1 mm was chosen.

The static pressure error can also be reduced by adjusting the orifice geometry. According to Erwin [17], a static pressure port which is rounded at the rear when facing flow direction (Fig. 20. (a)), diminishes the static pressure error by 0.5 %. Since this is difficult to manufacture, a geometry with an 82 ° slanted orifice (Fig. 20 (b)) was chosen, which reduces the error still by 0.3 %.

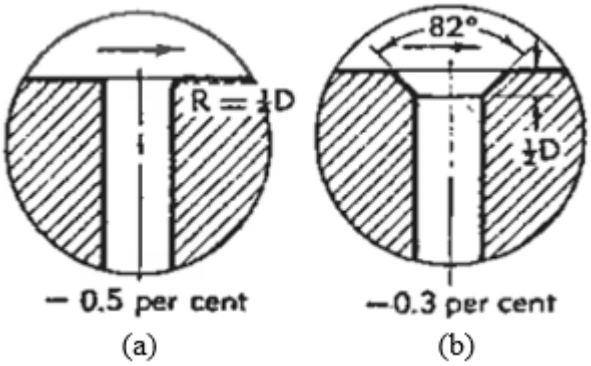

Fig. 20. Static pressure ports, with a rear rounded (a) and a slanted (b) orifice.

The total-pressure tubes of one unit are placed in a row and a spacing of 7 cm. Because flow direction diverts for every variation (e.g. pitch and sideslip angle of the aircraft), the total-pressure tube design is based on a study [18] of the National Advisory Committee for Aeronautics (NACA). Accordingly, the total-pressure tube has a cylindrical nose shape, an impact opening equal to the tube diameter and a 30° opening chamber (see Fig. 21). This design limits the total-pressure error to 1% up to a misalignment angle of 28°.

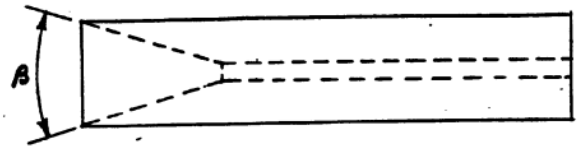

Fig. 21. Pitot tube design (cylindrical nose shape, impact opening equal to the tube diameter and a 30° opening chamber β), according to a study [18] of NACA for total-pressure tubes.

The velocity can be calculated with static pressure p_S and total pressure p_T (4). The value of density ρ is provided by the measurement system of the LWTE.

$$v = \sqrt{\frac{2 \cdot (p_T - p_S)}{\rho}} \qquad (4)$$

The flow speed measurement (static and total pressure) will be calibrated using a thermal flow meter. To do so, one measurement unit – which includes the duct part where the ports are installed – will be mounted in the smaller wind tunnel at the ZHAW - Zurich University of Applied Sciences, School of Engineering.

3.5 Tested scenarios

According to experienced aerobatic pilots, the angles of attack and side slip during an aerobatic exhibition do not exceed ±10 °. Therefore, the measurement program will include 1 ° steeped angle of attack sweeps for side slip angles of -10 °, -5 °, 0 °, 5 ° and 10 °.

These measurements will be repeated with wind tunnel flow speeds of 0 m/s, 30 m/s (stall speed of the aircraft) and 68 m/s and engine power settings of 0 %, 40 %, 60 % and 100 %.

4 Conclusion and outlook

In this paper, CHT simulations of convective heat transfer in the cooling air channel of an electric power plant installation were discussed. The mesh study determined a sufficient mesh size for the CHT analysis regarding the current geometry of the cooling duct. Further, a possible improvement in convective cooling with a turbulator pin fins matrix was investigated. The results match the theory from past research and confirm the potential of the turbulators to increase convective heat transfer performance. In the experimental part, the full scale wind tunnel tests set up has also been described. These planned tests aim on the one hand to deliver initial conditions at different flight attitudes for further numerical research, e.g. volume flow at inlet and outlet, and on the other hand to obtain experiment data for validation of entire numerical model (shown in Fig. 22).

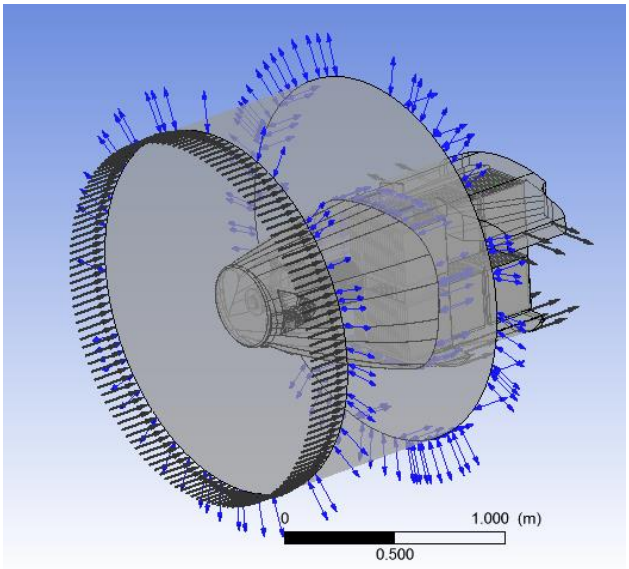

Fig. 22. Entire numerical model.

References

[1] Baehr D, Stephan K. *Wärme- und Stoffübertragung*, Springer Verlag, 2006.

[2] Liu X., Ferrari F, and Manfriani L**.** *Hybrid cooling of a high-performance electric propulsion system for aerobatic aircrafts*. Technical report, Hightech centre Aargau, 2017.

[3] Eifel M. *Experimental and numerical investigation of various geometries in convection cooled gas.* Dissertation, RWTH Aachen University, 2011.

[4] Menter F.R. Zontal two equation k-ω turbulence models for aerodynamic flows, *AIAA paper*, 93-2906, 1993.

[5] Menter F.R. Zontal two equation k-ω turbulence models for aerodynamic flows, *AIAA paper*, Vol.1, No.8, pp 1598-1605, 1994.

[6] ANSYS. *ANSYS meshing user's guide release 15.0 manual*, 2013.

[7] Deng G, Piquet J. Navier-Stokes computation of horseshoe vortex flows, *International journal for numerical methods in fluids*, 15, pp 99-124, 1992.

[8] York D, Piquet H, Holloway S. Prediction of heat transfer in a ribbed channel: evaluation of unsteady rans methodology, *Proceedings of ASME turboexpo*, GT2005-68821, 2005.

[9] Yang H, Chen H-C, Han J-C. Numerical prediction of film cooling and heat transfer with different film-hole arrangements on the plane and squealer tip of a gas turbine blade, *Proceedings of ASME turboexpo*, GT2005-68821, 2004.

[10] ANSYS. *ANSYS CFX release 18.0 manual*, 2017.

[11] Berni F, Fontanesi S. Integrated in-cylinder/CHT methodology for the simulation of the engine thermal field: an application to high performance turbocharged DISI Engine, *SAE International*, 2016-01-0578, 2016

[12] Wälti P. *Thermische Simulationen zur Optimierung der Anordnung der Batteriezellen für das elektrische Kunstflugzeug des Projektes evolaris.* Project work, Bern University of Applied Sciences, 2016.

[13] Armstrong J, Winstanley D. A review of staggered array pin fin heat transfer for turbine cooling applications, *Journal of turbomachinery*, 110(1), pp 94-103, 1988.

[14] Metzger D, Berry R, Bronson J. Developing heat transfer in rectangular ducts with staggered arrays of short pin fins, *Journal of turbomachinery*, 110(1), pp 94-103, 1982.

[15] DIN, E. N. 60751: 2009–05. *Industrielle Platin-Widerstandsthermometer und Platin-Temperatursensoren*, 2009.

[16] Rayle, R. E. *An investigation of the influence of orifice geometry on static pressure measurements.* Diss. Massachusetts Institute of Technology, 1949.

[17] Erwin, J. *Experimental techniques "Aerodynamics of Turbines and Compressors" (Section D), Vol. X of High Speed Aerodynamics and Jet Propulsion.* Princeton University Press, 1964.

[18] Gracey, W. *Wind-tunnel investigation of a number of total-pressure tubes at high angles of attack-subsonic, transonic, and supersonic speeds.* NACA-TN-3641. NATIONAL AERONAUTICS AND SPACE ADMINISTRATION HAMPTON VA LANGLEY RESEARCH CENTER, 1956.

6 Contact Author Email Address

mailto:liux@zhaw.ch

Copyright Statement